FACTA UNIVERSITATIS
Series: **Mechanical Engineering** Vol. 22, Nº 2, 2024, pp. 257 - 273
https://doi.org/10.22190/FUME240118033M

Original scientific paper

NONLINEAR DYNAMICAL CHARACTERISTICS OF HYBRID TRI-STABLE PIEZOELECTRIC ENERGY HARVESTER BASED ON ROTATIONAL MOTION

Da-Wei Man[1,2], Yu Zhang[1], Li-Ping Tang[1,2], Qing-Hu Xu[1,2], Dong Chen[1,2], Bang-Dong Jiang[1], Ting-Ting Han[1,2], Tao Xu[3], Jin-Bao Li[4]

[1]School of Civil Engineering, Anhui Jianzhu University, Hefei, China
[2]BIM Engineering Center of Anhui Province, Hefei, China
[3]China Construction First Group the Fifth Construction CO., Ltd, Beijing, China
[4]Jiangsu Southeast Special Engineering & Technology Co., Ltd, Nanjing, China

ORCID iDs: Da-Wei Man https://orcid.org/0000-0003-3053-2318
Yu Zhang https://orcid.org/0009-0006-4473-9183
Li-Ping Tang https://orcid.org/0009-0006-5184-4483
Qing-Hu Xu https://orcid.org/0000-0002-8617-8373
Dong Chen https://orcid.org/0009-0002-0221-9383
Bang-Dong Jiang https://orcid.org/0009-0003-0063-138X
Ting-Ting Han https://orcid.org/0009-0008-2379-214X
Tao Xu https://orcid.org/0009-0002-8384-1608
Jin-Bao Li https://orcid.org/0009-0009-0251-0665

Abstract. *The paper presents an improved hybrid tri-stable cantilever piezoelectric energy harvester based on rotational motion, thus providing a new perspective for achieving higher efficiency in energy capture for rotational motion. The proposed system comprises a piezoelectric cantilever beam with an innovative dynamic amplifier installed at the edge of a vehicle's wheel hub. Through theoretical analysis and numerical simulations, the influence of parameters such as the mass of the tip magnetic on the piezoelectric beam, the wheel hub radius, rotational speed, and the ratio of the dynamic amplifier's spring stiffness are investigated with respect to the system's steady-state dynamic response and time-domain performance. A comparative analysis is also conducted with traditional tri-stable piezoelectric energy harvesters. The results demonstrate that the hybrid tri-stable piezoelectric energy harvester exhibits superior performance in capturing vibrational energy during rotational motion, compared to traditional tri-stable piezoelectric energy harvesters. Proper adjustments to the mass of the tip magnetic and the internal spring stiffness of the dynamic amplifier can enhance the system's output voltage and the rotational speed range of inter-well motion. Additionally, the rotational speed range of inter-well motion increases with the expansion of the wheel hub radius. However, when the rotational speed is below 100 rpm, the influence of varying the wheel hub radius on the system's output voltage is minimal.*

Key words: *Rotational motion, Piezoelectric energy harvester, Tri-stable, Dynamic amplifier, Steady-state dynamic response*

Received: January 18, 2024 / Accepted May 22, 2024
Corresponding author: Da-Wei Man
School of Civil Engineering, Anhui Jianzhu University, Hefei 230601, China
E-mail: daweiman@hotmail.com

1. INTRODUCTION

The widespread application of wireless sensor networks in infrastructure monitoring, ecological environment monitoring, and disaster warning imposes higher requirements on the cleanliness and sustainability of their power sources. Traditional chemical batteries are toxic, have limited lifespans, and pose challenges such as time-consuming replacements, high costs, and difficulty in handling waste batteries [1-6]. Piezoelectric energy harvesters, capable of capturing vibrational energy from the surrounding environment and converting it into persistent and clean electrical energy, hold significant potential for self-powering wireless sensor nodes due to their simple, compact, and easily integrable structures. This has garnered extensive attention from scholars both domestically and internationally in recent years [7-12]. Early linear piezoelectric harvesters were restricted to generating high output power only in resonance, exhibiting low efficiency in wide-frequency or random vibrational environments. To overcome this limitation, researchers introduced nonlinearity to linear systems, resulting in nonlinear piezoelectric harvesters with broader operating frequency bands. This innovation renders them less sensitive to variations in external vibration frequencies, so that they are more suitable for effectively harvesting energy from diverse environmental vibrations [13, 14].

Stanton et al. [15, 16] established a magnetic non-linear bi-stable piezoelectric harvester composed of a permanent magnet and a piezoelectric cantilever beam. Under low-frequency vibrational excitations, it exhibits oscillations between two potential wells, significantly broadening the operating bandwidth and output power compared to linear piezoelectric harvesters. However, under low intensity vibrational, the bi-stable piezoelectric harvester may struggle to overcome potential energy barriers for substantial inter-well motion [17-20]. Consequently, researchers proposed nonlinear multi-stable piezoelectric harvesters, typically utilizing multiple magnets to create multiple potential wells. By adjusting system parameters, the barrier height between wells can be reduced, making it easier for the system to generate high-energy inter-well motion. Wang et al. [21] studied the influence mechanism of geometric nonlinearity and gravitational effects on the dynamic response of a tri-stable piezoelectric harvester through theoretical analysis and experimental methods. Zhu et al. [22] analyzed the impact of three potential well distribution characteristics on the energy harvesting performance of tri-stable piezoelectric harvesters, showing optimal performance when the barrier heights are equal. Yang et al. [23] investigated a hybrid tri-stable vibration energy harvester employing geometric nonlinearity to adjust the resonant frequency and expand the inter-well motion bandwidth. The results indicate that the tri-stable characteristic has the potential to enhance significantly the harvested power. Zhou et al. [24] proposed penta-stable cantilever beam piezoelectric harvesters to achieve greater deformation and higher output voltage.

Most studies on piezoelectric harvesters have focused on harmonic excitation. However, rotational motion is prevalent in both civilian and industrial environments. In recent years, some researchers have focused on using piezoelectric harvesters to achieve self-powering for sensor nodes in rotating machinery such as wheels and wind turbines [25,26]. Khameneifar et al. [27] designed a cantilever beam linear piezoelectric harvester that generates continuous vibration and harvests energy through the periodic excitation caused by the tip mass of the beam during rotational motion. Zhang et al. [28] proposed a bi-stable piezoelectric harvester mounted on the edge of a hub, capable of converting the rotational and kinetic energy generated by external excitation into electrical energy to power a tire

pressure monitoring system. Mei et al. [29] established a theoretical model of a magnetic tri-stable piezoelectric harvester based on rotational motion, analyzing the impact of different speeds and piezoelectric coupling coefficients on the system's energy harvesting efficiency.

Currently, effective broadening of the operating frequency band and improvement of the power performance of piezoelectric harvesters under different rotational radius and speeds remain urgent research issues. This paper designs a hybrid tri-stable piezoelectric harvester (HTPEH) by attaching a novel dynamic amplifier composed of rotational and vertical springs to the fixed end of a traditional cantilever piezoelectric beam. This amplifier simultaneously increases the rotational amplitude and vertical displacement of the cantilever beam during rotational motion. The influence of rotational radius, magnetic mass at the beam's end, and spring stiffness ratio on the steady-state dynamic response of the HTPEH under rotational motion is investigated.

2. Modeling of Hybrid Tri-Stable Piezoelectric Energy Harvester

Figure 1 depicts a HTPEH mounted on the edge of a vehicle wheel hub, with r being the radius of the wheel hub. In Fig. 2, a schematic illustration of the HTPEH during rotational motion is given. It features a piezoelectric cantilever beam, with l and b denoting the length and width of the beam, respectively. The free end of the beam is equipped with a tip magnetic denoted as A and a mass m_f is attached to the fixed end through rotational spring k_r and vertical spring k_f connecting the wheel hub edge and a L-shaped frame. The mass m_f combined with springs k_r and k_f constitutes a novel power amplifier, capable of simultaneously increasing the rotational amplitude and vertical displacement of the cantilever beam during rotational motion. The piezoelectric beam consists of a substrate layer with thickness h_s and two piezoelectric layers covering its upper and lower surfaces. The thickness of the substrate layer and piezoelectric layer are h_s and t_p. The external load resistance R_L is connected in series. Two external magnets, denoted in the figure by B and C, are arranged on the L-shaped frame, and their appropriate spacing with the tip magnetic tip induces a tri-stable potential energy function for the system.

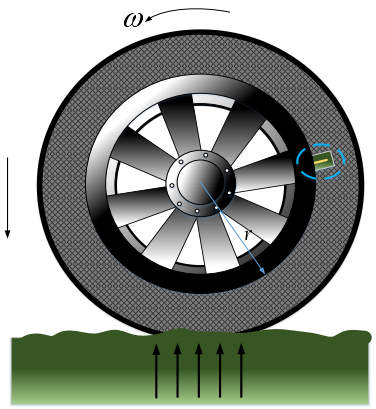

Fig. 1 The HTPEH installed on a vehicle wheel hub

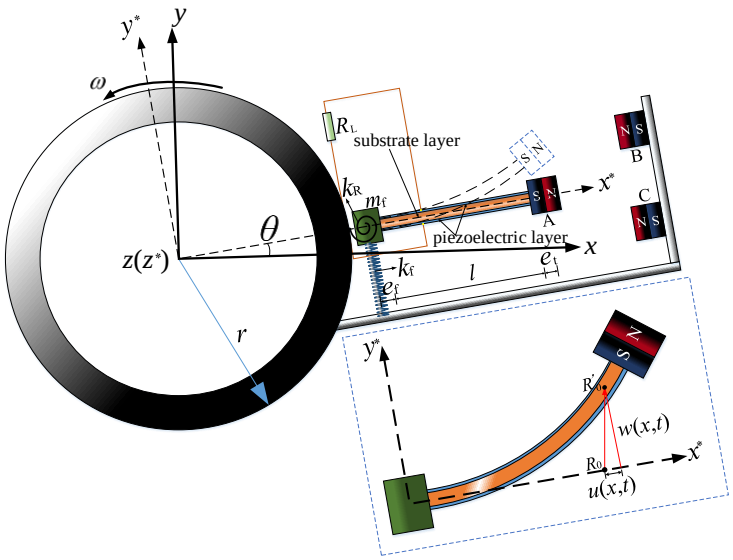

Fig. 2 The schematic diagram of the HTPEH in rotational motion

In Fig. 2, the *x*-*y*-*z* coordinates represent the fixed coordinate system, and *x**-*y**-*z** is the rotating coordinate system. Assuming R_0 defines the position of an infinitesimal segment *dx* on the beam in the rotating coordinate system, *w*(*x*,*t*) and *u*(*x*,*t*) denote the lateral and axial displacements at position *x* during beam vibration. The angle between the *x*-axis and the x^*-axis is defined by $\theta = \int_0^t \omega dt$, where ω is the angular displacement of the wheel hub. The eccentricities of the tip magnetic and the mass block m_f are denoted as e_t and e_f, respectively. The constitutive relationships for the metal base layer and piezoelectric layers of the piezoelectric beam are as follows:

$$\left.\begin{aligned} T_1^s &= Y_s S_1^s \\ T_1^p &= Y_p (S_1^p - d_{31} E_3) \\ D_3 &= d_{31} T_1 + \varepsilon_{33}^T E_3 \end{aligned}\right\} \tag{1}$$

Here, the subscript/superscript s represents the parameters associated with the substrate layer, while the subscript/superscript p represents those associated with the piezoelectric layer. The *x** and *y** directions are indicated by subscripts 1 and 3, respectively. *T*, *S*, and *Y* represent the stress, strain, and Young's modulus of the beam, respectively. D_3, d_{31}, and ε_{33}^T denote the electric displacement, piezoelectric constants, and dielectric constants, respectively. With *V*(*t*) denoting the voltage, the relation $E_3 = -V(t)/(2t_p)$ holds, where E_3 is the electric field. The relationship between the displacement and strain is expressed as $S_1^s = S_1^p = -yw''$, where *y* represents the distance between the neutral axis of the beam and the point on its cross-section.

The Lagrangian for the HTPEH is expressed as follows:

$$L = T - U + W_e \tag{2}$$

where T represents the kinetic energy of the system, U is the overall potential energy consisting of the strain energy, U_e, the gravitational potential energy, U_g, the centrifugal potential energy U_c, the strain energy, U_d, and the magnetic potential energy U_m. Finally, W_e represents the electrical energy of the system. Based on the geometric relationships presented in Fig. 1(b), the kinetic energy of the system can be expressed as:

$$\begin{aligned} T = & \frac{1}{2} m_0 \int_0^l \left\{ \dot{\theta}^2 w(x,t)^2 + \left[\dot{w}(x,t) + \left(x + r + u(x,t) \right) \dot{\theta} \right]^2 \right\} \mathrm{d}x \\ & + \frac{1}{2} m_\mathrm{f} \left\{ \dot{\theta}^2 w(0,t)^2 + \left[\dot{w}(0,t) - e_\mathrm{f} \dot{w}'(0,t) + \left(r + u(0,t) \right) \dot{\theta} \right]^2 \right\} \\ & + \frac{1}{2} m_\mathrm{t} \left\{ \dot{\theta}^2 w(l,t)^2 + \left[\dot{w}(l,t) + e_\mathrm{t} \dot{w}'(l,t) + \left(l + r + u(l,t) \right) \dot{\theta} \right]^2 \right\} \\ & + \frac{1}{2} J_\mathrm{f} \dot{w}'(0,t)^2 + \frac{1}{2} J_\mathrm{t} \dot{w}'(l,t)^2 \end{aligned} \tag{3}$$

The strain energy of the system can be expressed as:

$$U_\mathrm{e} = \frac{1}{2} \int_0^l \left[YIw''(x,t)^2 - \frac{1}{2} Y_\mathrm{p} b d_{31} (h_\mathrm{s} + t_\mathrm{p}) V(t) w''(x,t) \right] \mathrm{d}x \tag{4}$$

where $YI = \frac{2}{3}\left[Y_s b h^3 + Y_p b\left(3h^2 t_p + 3h{t_p}^2 + {t_p}^3\right)\right]$ represents the bending stiffness of the beam.

The gravitational potential energy of the system is given by:

$$U_\mathrm{g} = m_0 g \int_0^l \left[(x+r)\sin\theta + w(x,t)\cos\theta \right] \mathrm{d}x + m_\mathrm{t} g \left[r\sin\theta + w(0,t)\cos\theta \right] + m_\mathrm{t} g \left[(l+r)\sin\theta + w(l,t)\cos\theta \right] \tag{5}$$

The centrifugal potential energy of the system in rotational motion is given by:

$$U_\mathrm{c} = \frac{1}{2} \int_0^l [m_0 r\dot{\theta}^2 (l-x) + \frac{1}{2} m_0 \dot{\theta}^2 (l^2 - x^2) + m_\mathrm{t} r\dot{\theta}^2 + m_\mathrm{t} \dot{\theta}^2 (l+r)] w'(x,t)^2 \mathrm{d}x \tag{6}$$

The strain potential energy of the dynamic amplifier is given by:

$$U_\mathrm{d} = \frac{1}{2} k_\mathrm{r} w'(0,t)^2 + \frac{1}{2} k_\mathrm{f} w(0,t)^2 \tag{7}$$

The electrical energy of the system is given by:

$$W_e = \tfrac{1}{4} Y_p b d_{31} \left(h_s + t_p\right) V(t) \int_0^l w''(x,t) dx + bl\varepsilon_{33}^S \frac{V(t)^2}{4t_p} \tag{8}$$

where, $\varepsilon_{33}^S = \varepsilon_{33}^T - d_{31}^2 Y_p$.

Utilizing the Galerkin method, the latera displacement $w(x,t)$ is expressed as:

$$w(x,t) = \sum_{r=1}^{n} \phi_r(x) q_r(t) \tag{9}$$

Here, $\phi_r(x)$ and $q_r(t)$ represent the r^{th} order modal shape function and generalized coordinate of the beam, respectively. The orthogonality condition for the modal shape functions is:

$$\begin{aligned} & \int_0^l \phi_s(s) m_0 \phi_r(s) \mathrm{d}s + \phi_s(l) m_\mathrm{t} \phi_r(l) + \phi_s(l) m_\mathrm{t} e_\mathrm{t} \phi_r'(l) + \phi_s'(l)(J_\mathrm{t} + m_\mathrm{t} {e_\mathrm{t}}^2) \phi_r'(l) + \phi_s'(l) m_\mathrm{t} e_\mathrm{t} \phi_r(l) \\ & + \phi_s(0) m_\mathrm{f} \phi_r(0) - \phi_s(0) m_\mathrm{f} e_\mathrm{f} \phi_r'(0) + \phi_s'(0)(J_\mathrm{f} + m_\mathrm{f} {e_\mathrm{f}}^2) \phi_r'(0) - \phi_s'(0) m_\mathrm{f} e_\mathrm{f} \phi_r(0) = \delta_{rs} \end{aligned} \tag{10}$$

$$\int_0^l \frac{\mathrm{d}^2\phi_s(s)}{\mathrm{d}s^2} YI \frac{\mathrm{d}^2\phi_r(s)}{\mathrm{d}s^2}\mathrm{d}s + \phi_m'(0)k_{\mathrm{R}}\phi_r'(0) + \phi_m(0)k_{\mathrm{f}}\phi_r(0) = \omega_r{}^2\delta_{rs} \tag{11}$$

where, δ_{rs} is the Kronecker delta function. The natural frequency of undamped vibration for the beam is given by $\omega_r = \lambda_r^2\sqrt{YI/(ml^4)}$, where λ_r is the eigenvalue. The computational method for λ_r and the mode shape functions has been presented by Man et al. [30]. Considering only the first-order mode, based on the author's previous research, the expression for magnetic potential energy, accounting for the eccentricity of the magnet at the beam tip, is given by:

$$U_{\mathrm{m}} = k_0 - \frac{1}{2}k_1 q_1{}^2 + \frac{1}{4}k_2 q_1{}^4 + \frac{1}{6}k_3 q_1{}^6 + o(q_1{}^7) \tag{12}$$

The expressions for the coefficients in the equation can be found in reference [30]. Considering only the first-order mode, substituting Eq. (9) into Eq. (2) and then into the following Lagrangian variational equation:

$$\begin{cases} \dfrac{\mathrm{d}}{\mathrm{d}t}\left(\dfrac{\partial L}{\partial \dot{q}}\right) - \dfrac{\partial L}{\partial q} = P(t) \\ \dfrac{\mathrm{d}}{\mathrm{d}t}\left(\dfrac{\partial L}{\partial \dot{V}}\right) - \dfrac{\partial L}{\partial V} = Q(t) \end{cases} \tag{13}$$

where, $P(t) = -2\xi_1\omega_1\dot{\eta}_1(t)$ represents the generalized dissipative force of the system, ω_1 is the first-order natural frequency of the system, ξ_1 is the damping ratio of the system, $Q(t)$ represents the generalized output charge, and $\dot{Q}(t) = -V(t)/R_L$, Utilizing Eq. (13), the electromechanical equation of the HTPEH can be derived as follows:

$$\ddot{q}_1 + 2\xi_1\omega_1\dot{q}_1 + \omega_1{}^2 q_1 + K_{\mathrm{c}}\dot{\theta}^2 q_1 - k_1 q_1 + k_2 q_1{}^3 + k_3 q_1{}^5 + \chi\ddot{\theta} - \vartheta V = \left[-\Gamma \mathrm{g} + F(t)\right]\cos\theta \tag{14}$$

$$C_{\mathrm{p}}\dot{V} + \frac{V}{R_{\mathrm{L}}} + \vartheta\dot{q} = 0 \tag{15}$$

In Eqs. (14) and (15), the expressions for the coefficients K_c, χ, ϑ, Γ and C_p can be found in the appendix, while $F(t)$ represents the external excitation arising from the interaction between the vehicle wheel and the road surface.

By introducing dimensionless parameters $S(\tau) = q_1(t)/l$, $\tau = \omega_1 t$, $\bar{V}(\tau) = VC_p/(l\vartheta)$ into Eqs. (14) and (15), we obtain:

$$\ddot{S} + 2\xi_1\dot{S} + (1 - K_1 + K_{\mathrm{c}}\omega^2)S + K_2 S^3 + K_3 S^5 + \bar{\chi}\ddot{\theta} - \Theta\bar{V} = \left[\bar{\Gamma}g + f(t)\right]\cos\omega\tau \tag{16}$$

$$\dot{\bar{V}} + \alpha\bar{V} + \dot{S} = 0 \tag{17}$$

where, $K_1 = k_1/\omega_1{}^2$, $\omega = \dot{\theta}/\omega_1$, $K_2 = k_2 l^2/\omega_1{}^2$, $K_3 = k_3 l^4/\omega_1{}^2$, $\bar{\chi} = \chi/l$, $\bar{\Gamma} = \Gamma/(l\omega_1{}^2)$, $f(t) = F(t)/(l\omega_1{}^2)$,$\Theta = \vartheta^2/(C_p\omega_1{}^2)$.

This study primarily investigates the rotational motion performance of HTPEH under various constant speeds in the absence of external excitations. Therefore, let $\ddot{\theta} = 0$, $f(t) = 0$,

considering the system's own gravity $\bar{\Gamma} g$ as an external excitation force F, then Eq. (16) can be rewritten as:

$$\ddot{S} + 2\xi_1 \dot{S} + (1 - K_1 + K_c \omega^2) S + K_2 S^3 + K_3 S^5 - \Theta \bar{V} = F \cos \omega \tau \tag{18}$$

3. Theoretical Analysis by Harmonic Balance Method

The solutions of Eqs. (18) and (17) may be assumed in the following form:

$$\begin{cases} S(\tau) = A(\tau)\sin(\omega\tau) + B(\tau)\cos(\omega\tau) \\ \bar{V}(\tau) = C(\tau)\sin(\omega\tau) + D(\tau)\cos(\omega\tau) \end{cases} \tag{19}$$

Substituting Eq. (19) into Eq. (17) and balancing the coefficients of the $\sin(\omega\tau)$ and $\cos(\omega\tau)$ terms, for steady-state motion, setting all time derivatives to zero, yields:

$$\begin{cases} C = \dfrac{\omega}{\omega^2 + \alpha^2}\left(B\alpha - \omega A\right) \\ D = \dfrac{\omega}{\omega^2 + \alpha^2}\left(-A\alpha - \omega B\right) \end{cases} \tag{20}$$

Substituting Eqs. (19) and (20) into Eq. (18), and repeating the above calculations while neglecting higher-order harmonic terms, we obtain:

$$-\omega^2 A - 2\omega\xi B + (1 - K_1 + K_c\omega^2)A + \frac{3K_2}{4}(A^3 + AB^2) + \frac{5K_3}{8}(A^5 + 2A^3B^2 + AB^4) - \frac{\Theta\omega}{\omega^2 + \alpha^2}\alpha B + \frac{\Theta\omega^2}{\omega^2 + \alpha^2}A = 0 \tag{21}$$

$$-\omega^2 B + 2\omega\xi A + (1 - K_1 + K_c\omega^2)B + \frac{3K_2}{4}(A^2B + B^3) + \frac{5K_3}{8}(A^4B + 2A^2B^3 + B^5) + \frac{\Theta\omega}{\omega^2 + \alpha^2}\alpha A + \frac{\Theta\omega^2}{\omega^2 + \alpha^2}B = F \tag{22}$$

Let the displacement amplitude of the system's steady-state motion be $a = \sqrt{A^2 + B^2}$, The voltage amplitude is $u = \sqrt{C^2 + D^2}$. Squaring both sides of Eqs. (21) and (22), and adding them together, we obtain:

$$a^2\left[-\omega^2 + \left(1 - K_1 + K_c\omega^2\right) + \frac{3K_2}{4}a^2 + \frac{5K_3}{8}a^4 + \frac{\Theta\omega^2}{\omega^2 + \alpha^2}\right]^2 + a^2\left[2\omega\xi + \frac{\Theta\omega}{\omega^2 + \alpha^2}\alpha\right]^2 = F^2 \tag{23}$$

Therefore, the steady-state displacement amplitude of the HTPEH in rotational motion can be determined by Eq. (23), and the expression for the steady-state output voltage amplitude is

$$u = \frac{\omega}{\sqrt{\omega^2 + \alpha^2}}a \tag{24}$$

4. Dynamic Response Analysis

In the first part of this section, analytical solutions for the HTPEH system are obtained using the harmonic balance method. The study investigates the influence of parameters such as the masses of the two ends of the beam, rotational radius, rotational speed, and the

stiffness ratio of the springs on the steady-state response of the HTPEH system during rotational motion. The correctness of the analytical solutions is verified through frequency sweep simulations.

In the second part, the system's energy harvesting performance in the time domain is analyzed using the ode45 solver in MATLAB. The geometric and material parameters for the HTPEH are given in Table 1.

Figures 3-5 depict the variations in steady-state displacement and output voltage amplitude of the HTPEH compared to the TPEH with different values of the m_t as the rotational speed changes when m_t = 25 g, m_f = 100 g, r = 0.21 m. The solid lines represent the analytical solutions of the HTPEH, the scattered points represent the analytical solutions of the TPEH, and the shaded regions represent the numerical solutions obtained by rotational speed sweeping of the HTPEH. From Fig. 3, it can be observed that both HTPEH and TPEH can generate significant inter-well motion during rotational motion influenced by their respective gravity. Compared to TPEH, HTPEH exhibits a significantly higher peak value of output voltage and inter-well motion range. As seen from Figs. 3 to 5, with the increase of the m_t, the displacement, output voltage and inter-well motion range of both piezoelectric harvesters increase significantly, and the energy harvesting advantage of HTPEH becomes more significant. When m_t = 25 g, the peak voltage and inter-well motion range of HTPEH increase by 11.85% and 29.26%, respectively, compared to TPEH. When m_t = 27.5 g, these two indicators increase to 11.95% and 29.50%, respectively, and when m_t = 30 g, they further increase to 12.34% and 30.42%. The larger m_t, the more significant the increase in peak voltage and inter-well motion range. Moreover, it can be observed that the numerical simulation results of the steady-state displacement and output voltage amplitude of HTPEH under different rotational speeds by rotational speed sweep are in good agreement with the analytical solutions obtained by the harmonic balance method.

Table 1 The geometry and material parameters of HTPEH

Parameters	Symbol	Value
Piezoelectric film length	l	80 mm
Piezoelectric film width	b	20 mm
Piezoelectric film thickness	h_s	0.2 mm
Young's modulus of the metal substrate	Y_s	70 GPa
Density of the metal substrate	ρ_s	2700 kg/m^3
Density of the piezoelectric layer	ρ_p	7750 kg/m^3
Magnetization intensity	M_A, M_B, M_C	1.22×10^{6} A/m
Magnetic volume	V_A, V_B, V_C	1.0×10^{-6} m^{-3}
Damping ratio	ε_1	0.01
Young's modulus of the piezoelectric layer	Y_p	60.98 GPa
Piezoelectric strain constant	d_{31}	-1.71×10^{-10} C/N
Dielectric constant of the metal substrate	ε^s_{33}	-1.33×10^{-8} F/m
Transverse distance of the magnet	d_h	18 mm
Vertical distance of the magnet	d_v	9 mm

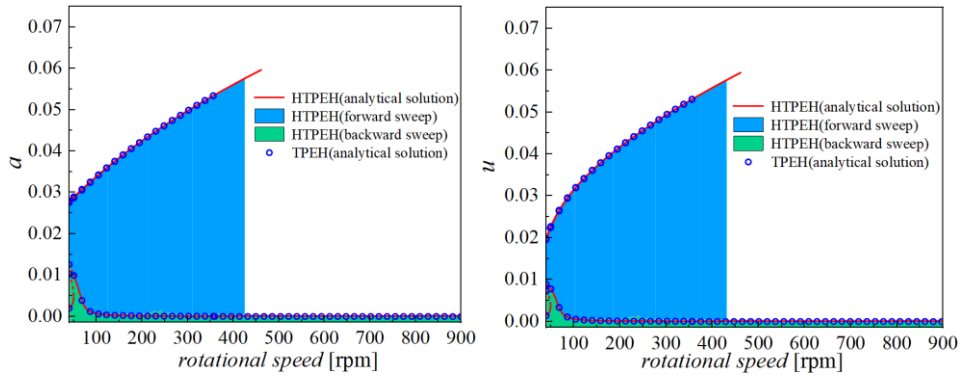

Fig. 3 a) Dependency of the dimensionless displacement and b) voltage amplitude of the system on the rotational speed for different models and $m_t = 25$ g

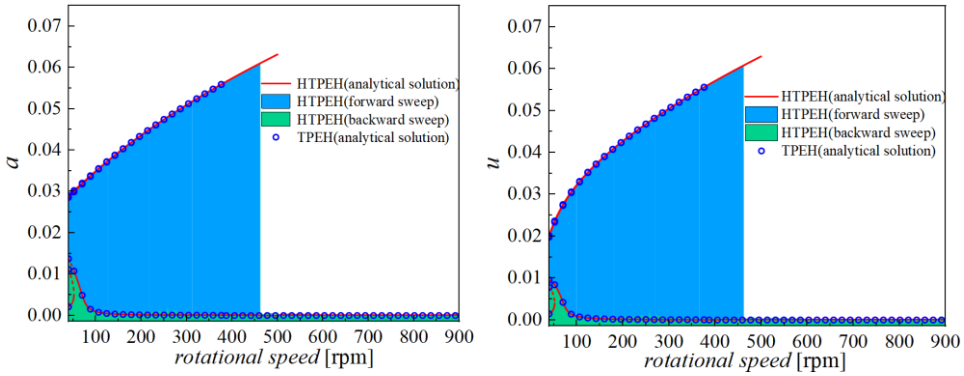

Fig. 4 a) Dependency of the dimensionless displacement and b) voltage amplitude of the system on the rotational speed for different models and $m_t = 27.5$ g

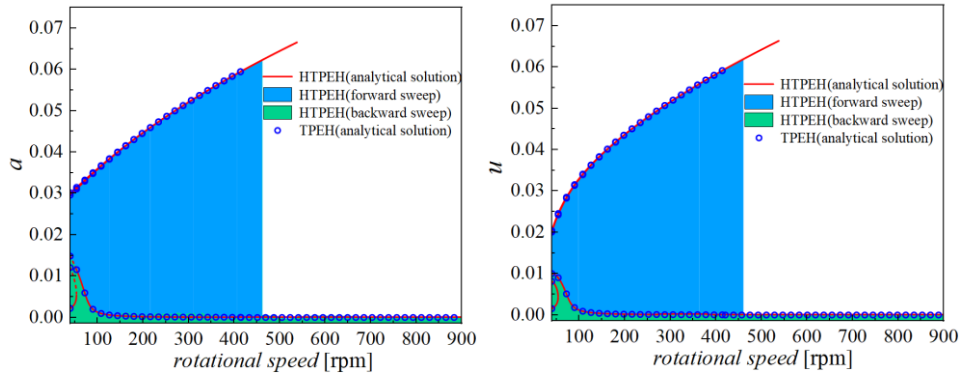

Fig. 5 a) Dependency of the dimensionless displacement and b) voltage amplitude of the system on the rotational speed for different models and $m_t = 30$ g

Figure 6 presents the curves of steady-state displacement and voltage amplitude with rotational speed for different values of the spring stiffness ratio $\bar{k} = k_f/k_r$, when m_t = 25 g and r = 0.21 m. It can be observed from Fig. 6 that the output voltage-rotational speed response curves for the three k_f/k_r ratios are essentially overlapping, while the steady-state output displacement, peak voltage and rotational speed range of inter-well motion all increase as k_f/k_r decreases.

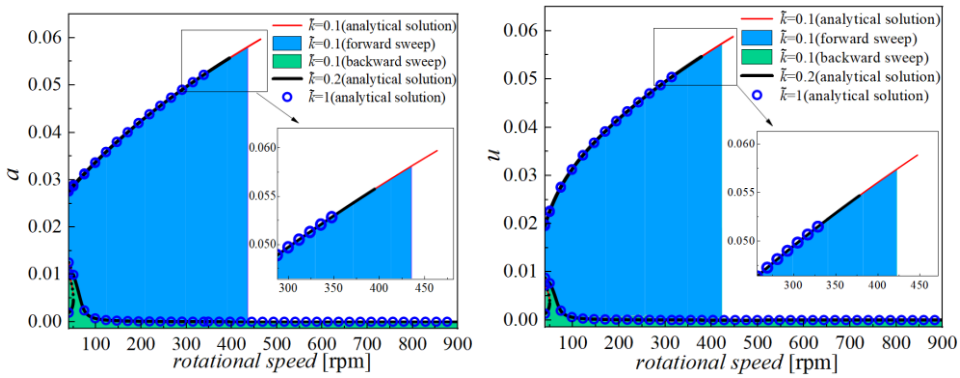

Fig. 6 a) Dependency of the dimensionless displacement and b) voltage amplitude response curves on the rotational speed for different spring stiffness ratios

To investigate the time-domain dynamic performance of HTPEH and TPEH at different wheel hub rotational speeds, Fig. 7 shows the phase diagram and voltage time-history diagram for both piezoelectric harvesters at 300 rpm when m_t = 25 g, m_f = 100 g, r = 0.21 m. It can be observed from Fig. 7 that HTPEH quickly transitions from intra-well motion to significant inter-well motion and generates a high output voltage after a short period of intra-well motion. In contrast, TPEH cannot overcome the potential barrier, only exhibiting small oscillations within the intra-wel, resulting in a small output voltage. This indicates that at the same rotational speed, HTPEH is more likely to escape the potential well and enter significant inter-well motion.

As the rotational speed increases to 350 rpm, it can be seen from Fig. 8 that HTPEH instantly enters a high-energy orbit to perform substantial inter-well motion, generating a large output voltage. On the other hand, TPEH, after a period of chaotic motion, eventually overcomes the potential barrier and escapes the well, entering significant inter-well motion with a longer time duration and a lower output voltage than HTPEH. In summary, at lower rotational speeds, HTPEH is more likely to break free from the potential well, generating higher output voltages and capturing more energy during rotational motion, demonstrating the advantages of HTPEH in energy harvesting performance.

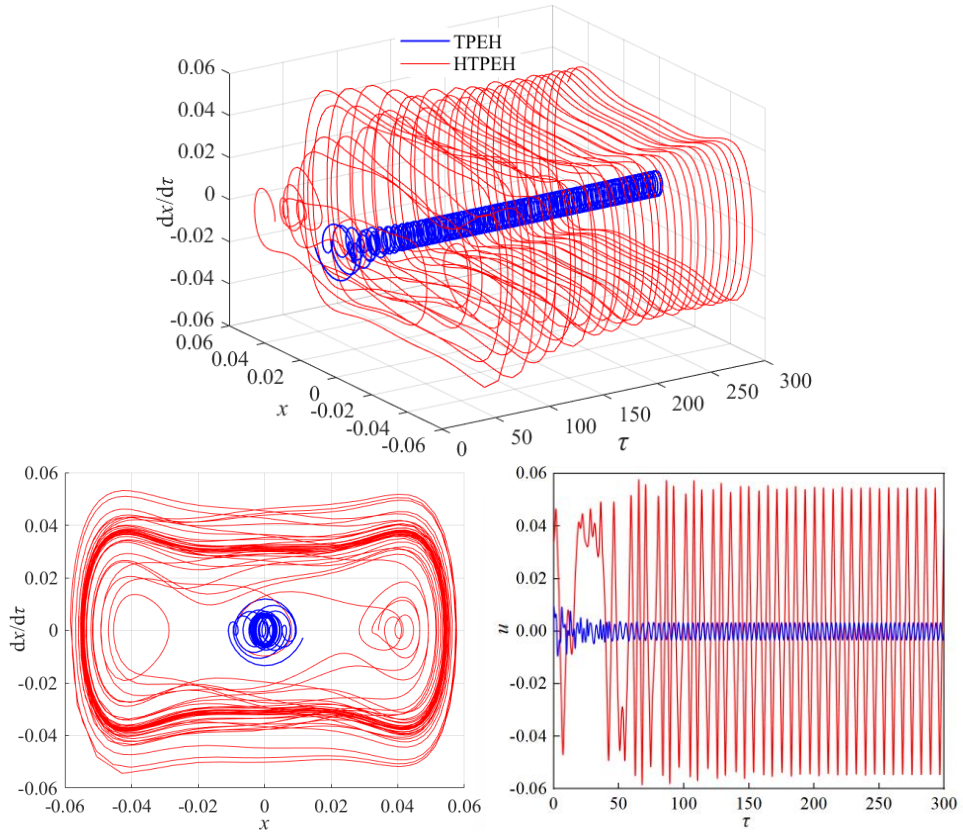

Fig. 7 (a) Three-dimensional phase diagram, (b) two-dimensional phase diagram, and (c) voltage time-history diagram for HTPEH and TPEH with the rotational speed of 300 rpm

Figure 9 presents the curves of the steady-state displacement amplitude and steady-state output voltage amplitude of HTPEH at different rotational radii with varying speeds when m_t = 25 g, m_f = 100 g. It can be observed that when the rotational speed is below 100 rpm, the change in rotational radius has a minimal impact on the steady-state displacement output voltage amplitude of HTPEH. However, when the speed exceeds 100 rpm, both the steady-state displacement output voltage amplitude decrease with an increase in the rotational radius. Moreover, as the rotational radius becomes larger, the decrease in amplitude becomes more pronounced.

Taking the peak value of the inter-well motion displacement under different rotational radii as an example, when the rotational radius is between 0.18 m and 0.33 m, the peak voltage of HTPEH shows a slow decline with an increase in rotational radius, and the corresponding inter-well motion range slowly increases. When the rotational radius is between 0.33 m and 0.37 m, the peak voltage of HTPEH sharply decreases with an increase in the rotational radius, and the corresponding inter-well motion range sharply increases. When the rotational radius is greater than 0.33 m, both the displacement and voltage peak values are observed to be at a very low level. This is because at this rotational radius, the HTPEH is restricted to intra-well motion.

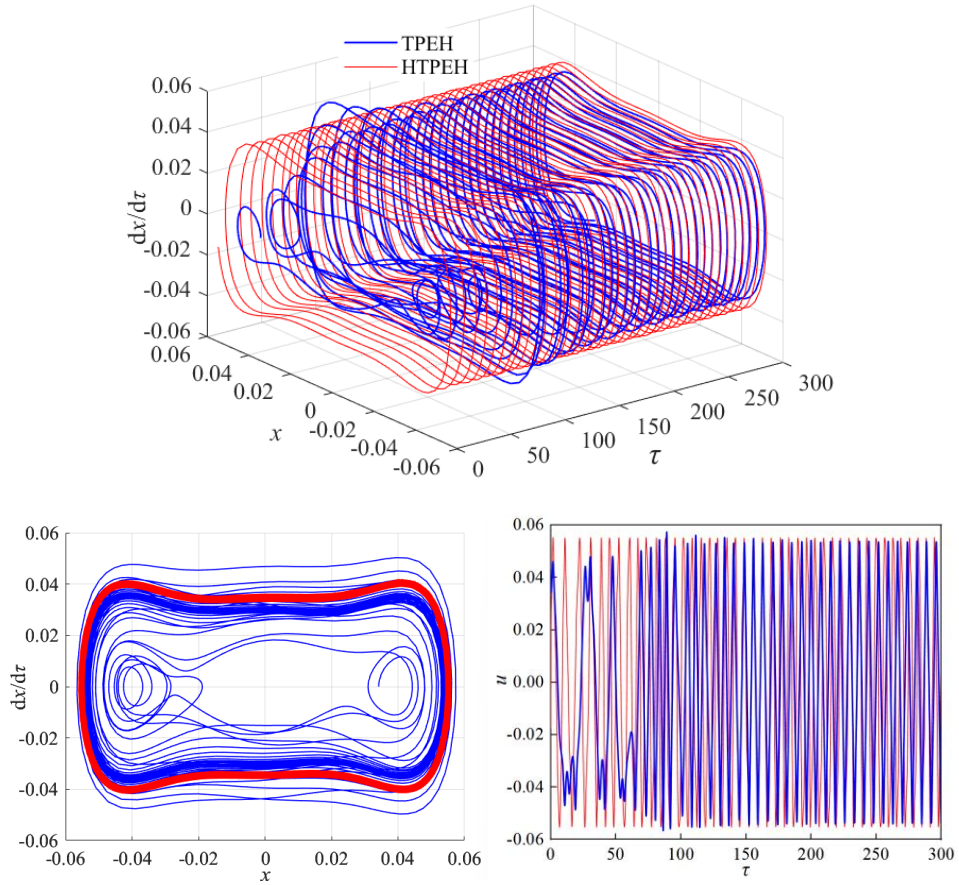

Fig. 8 (a) Three-dimensional phase diagram, (b) two-dimensional phase diagram, and (c) voltage time-history diagram for HTPEH and TPEH with the rotational speed of 350 rpm

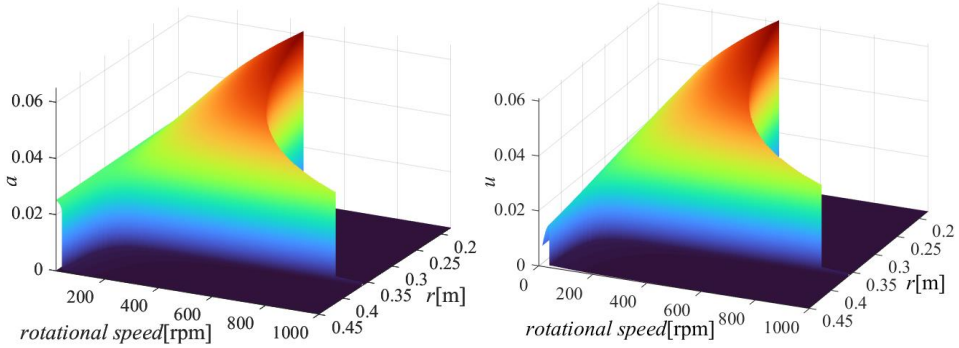

Fig. 9 Dependency of the dimensionless a) displacement amplitude and (b) the voltage amplitude on rotational speed for HTPEH and different rotational radii

Although increasing the rotational radius leads to a decrease in the peak voltage of HTPEH, it simultaneously increases the range of inter-well motion. Consequently, the system can capture energy from rotational motion over a broader speed range. Therefore, an appropriate radius should be set based on practical considerations such as the installation position, the dimensions and the specific application requirements of HTPEH.

Figure 10 depicts the phase portraits and voltage-time history diagram for HTPEH at a rotational speed of 300 rpm, with wheel hub radii corresponding to r = 0.18 m and r = 0.21 m. It can be observed that when r = 0.18 m, the system undergoes a period of chaotic motion, subsequently overcoming the potential barrier to perform significant inter-well motion and generating a higher output voltage. At r = 0.21 m, the system cannot overcome the potential barrier, remaining in small oscillations within one well and unable to enter inter-well motion, resulting in only a small output voltage. As the rotational increases to 350 rpm, as shown in Fig. 11, HTPEH under both r = 0.18 m and r = 0.21 m can generate inter-well motion. However, the system with the smaller rotational radius requires less time to enter inter-well motion. When the system with a rotational radius of

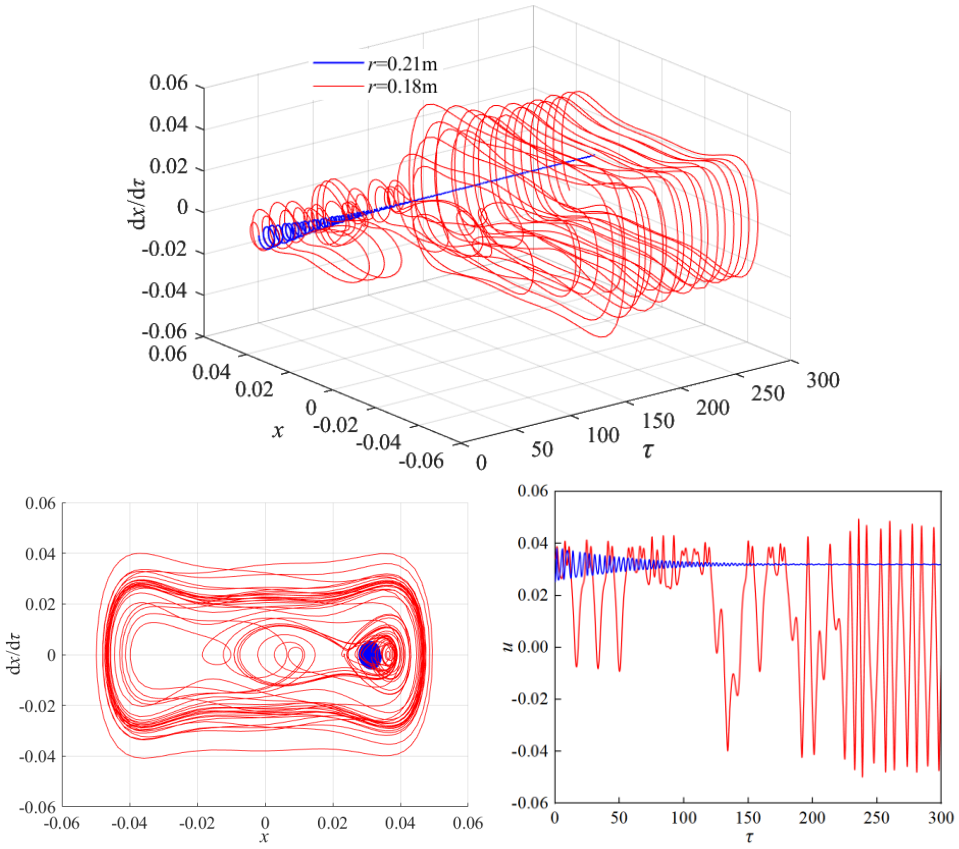

Fig. 10 (a) Three-dimensional phase diagram, (b) two-dimensional phase diagram, and (c) voltage-time history diagram for HTPEH with different values of wheel hub radius at a rotational speed of 300 rpm

r = 0.21 m enters stable inter-well motion, its output voltage is significantly lower than that of the system with the rotational radius of r = 0.18 m. Figures 9 and 10 illustrate that reducing the rotational radius or increasing the rotational speed can make the HTPEH more easily enter substantial inter-well motion, resulting in stable output voltage.

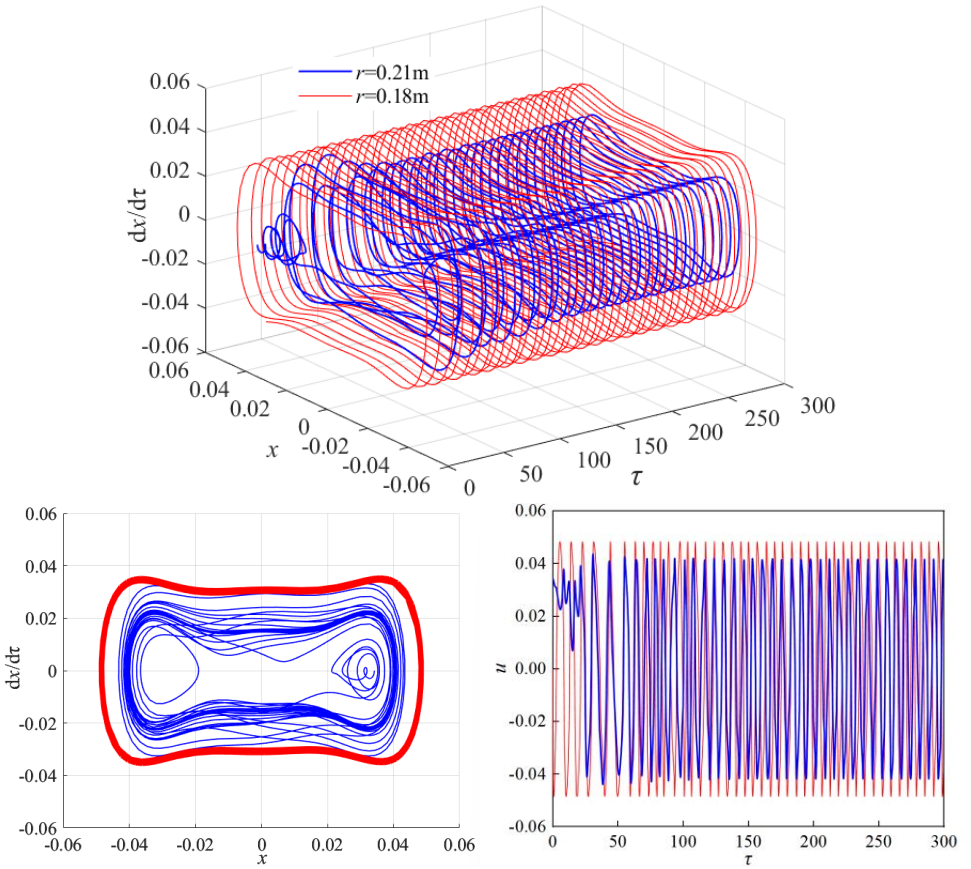

Fig. 11 (a) Three-dimensional phase diagram, (b) two-dimensional phase diagram, and (c) voltage-time history diagram for HTPEH with different values of wheel hub radius at a rotational speed of 350 rpm

Figures 12 and 13 show the output power amplitude curves of the system at various rotational speeds with different load resistances for rotational radii of r = 0.21 m and r = 0.36 m, respectively. It is evident that for HTPEH with different rotational radii, substantial inter-well motion can only be generated within a certain rotational speed range. Beyond a certain rotational speed, the system transitions into intra-well motion, resulting in a very small output power, and the rotational speed range conducive to inter-well motion generation expands with an increase in the wheel hub radius.

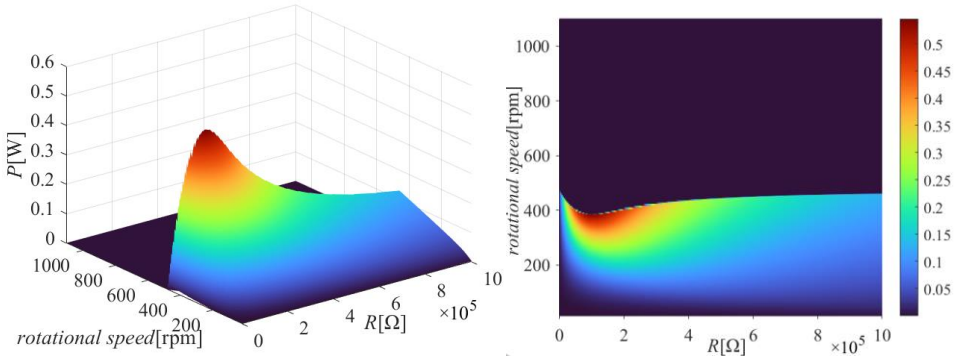

Fig. 12 a) The variation surface and b) top view of the impact of resistance on the system's output power at the wheel hub radius of 0.21 m

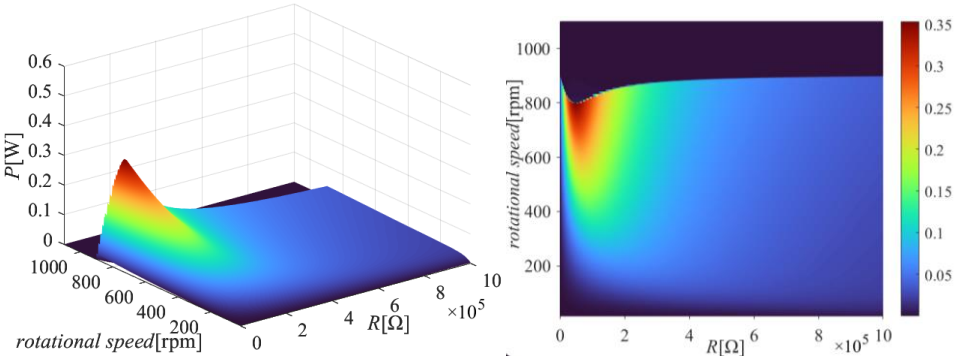

Fig. 13 a) The variation surface and b) top view of the impact of resistance on the system's output power at the wheel hub radius of 0.36 m

5. Conclusion

This paper introduces a hybrid tri-stable piezoelectric energy harvester based on rotational motion. The dynamic model of the system is established using Lagrangian equations. The influence of various factors such as the mass of the piezoelectric beam tip magnet, wheel hub radius, rotational speed, and the stiffness ratio of the dynamic amplifier on the system's steady-state dynamic response is analyzed. A comparison with traditional tri-stable piezoelectric energy harvesters is conducted. The theoretical analysis is validated through rotational sweep numerical simulations, and the system's time-domain dynamic performance is analyzed using the MATLAB software. The main conclusions from the theoretical analysis and numerical simulations are as follows:

- Compared to traditional tri-stable piezoelectric energy harvesters without a dynamic amplifier, the hybrid tri-stable piezoelectric energy harvester exhibits significantly improved output voltage and inter-well motion range during rotational motion.
- At lower speeds, changes in wheel hub radius minimally affect the HTPEH system's output voltage. While the range of inter-well motion expands with an increase in wheel hub radius, but there is a concurrent decrease in peak output voltage.

- Increasing the mass of the tip magnet or reducing the stiffness ratio of the vertical spring to the rotational spring can simultaneously increase the HTPEH system's output voltage amplitude and range of inter-well motion.
- At higher rotational speeds or smaller wheel hub radii, the HTPEH is more likely to enter large inter-well motion, resulting in higher output voltage.

Acknowledgment: *This research was funded by the Anhui Provincial University Provincial Natural Science Research Project-Key Project (2022AH050240), the Doctoral Startup Foundation of Anhui Jianzhu University (2020QDZ07), the Scientific research Project of Anhui Education Department-Key Project(KJ2021JD01), the Anhui Provincial Natural Science Foundation (2108085MA28), the Mechanical Properties Research of FRP Connectors in Fabricated Concrete Sandwich Insulation Wall Panels after Fire (KJ2021A0608), the Anhui Provincial Course Ideological and Political Demonstration Course(2022kcsz060).*

REFERENCES

1. Panchal, R.A., Koratkar, N.A., 2024, *Energy harvesting from water flow through porous reduced graphene oxide networks*, The Journal of Engineering, 2024(1), e12338.
2. Khalil, A.R., Hussain, M.I., Shah, M.H., Muhimeed, T. I., Nazir, G., Hussain, F., Mumtaz, U., 2024, *The exp loration of physical properties of 2D MXenes M3N2 (M= Ti, Hf, Zr, Mo) through the first principles approac h: The energy harvesting materials*, Computational Materials Science, 238, 112947.
3. Chatterjee, R., Shah, C.L., Gupta, S., Sarkar, S., 2024, *Energy harvesting in a flow-induced vibrating flapper with biomimetic gaits*, International Journal of Mechanical Sciences, 272, 109150.
4. Ullah, N., Islam, M.S., Hoque, A., Kirawanich, P., Alamri, S., Alsaif, H., Islam, M. T., 2024, *Compact dual-band metamaterial absorber: Enhancing electromagnetic energy harvesting with polarization-insensitive an d wide-angle capabilities*, Optics and Laser Technology, 175, 110829.
5. Khatun, H., Sharma, C., Sarma, U., 2024, *Investigation of ambient vibration sources for direct energy harvesting by optimizing resonant frequency using proof mass*, Measurement Science and Technology, 35, 055101.
6. Saurabh, N., Limbore, S., Kuldeep, H., Patel, S., 2024, *Simulation and experimental study of NBT-BT based compositions for thermal energy harvesting*, Materials Today Communications, 38, 108331.
7. Erturk, A., Inman, D.J., 2011, *Broadband piezoelectric power generation on high-energy orbits of the bistableDuffing oscillator with electromechanical coupling*, Journal of Sound and Vibration, 330(10), pp. 2339-2353.
8. He, J.H., Abd Elazem, N.Y., 2022, *The carbon nanotube-embedded boundary layer theory for energy harvesting*, Facta Universitatis-Series Mechanical Engineering, 20(2), pp. 211-235.
9. Stepancikova, R., Olejnik, R., Matyas, J., Masar, M., Hausnerova, B., Slobodian, P., 2024, *Pressure-Driven Piezoelectric Sensors and Energy Harvesting in Biaxially Oriented Polyethylene Terephthalate Film*, Sensors, 24(4), 1275.
10. Anang, F.E.B., Wei, X., Xu, J., Cain, M., Li, Z., Brand, U., Peiner, E., 2024, *Area-Selective Growth of Zinc Oxide Nanowire Arrays for Piezoelectric Energy Harvesting*, Micromachines, 15(2), 261.
11. Golabek, J., Strankowski, M., 2024, *A Review of Recent Advances in Human-Motion Energy Harvesting Nanogenerators, Self-Powering Smart Sensors and Self-Charging Electronics*, Sensors, 24(4), 1069.
12. Manoujan, A.Z., Riasi, A., 2024, *Optimal selection of parallel pumps running as turbines for energy harvesting in water transmission lines considering economic parameters*, Applied Energy, 359, 122687.
13. Qian, F., Zhou, S.X., Zou, L., 2020, *Approximate solutions and their stability of a broadband piezoelectric energy harvester with a tunable potential function*, Communication in Nonlinear Science and Numerical Simulation, 80, 104984.
14. Liu, H.C., Fu, H.L., Sun, L.N., Lee, C.K., Yeatman, E.M., 2020, *Hybrid energy harvesting technology: from materials, structural design,system integration to applications*, Renew and Sustainable Energy Reviews, 137, 110473.
15. Stanton, S.C., McGehee, C.C., Mann, B.P., 2010, *Nonlinear dynamics for broadband energy harvesting: investigation of a bistable piezoelectric inertial generator*, Physica D, 239, pp. 640-653.

16. Stanton, S.C., Erturk A., Mann, B.P., Inman, D.J., 2010, *Nonlinear piezoelectricity in electroelastic energy harvesters: modeling and experimental identification*, Journal of Applied Physics, 108, 074903.
17. Zhou, S.X., Cao, J.Y., Inman, D.J., Lin, J., Liu, S.S., Wang, Z.Z., 2014, *Broadband tristable energy harvester: modeling and experiment verification*, Applied Energy, 133, pp. 33-39.
18. Cao, J.Y., Zhou, S.X., Wang, W., Lin, J., 2015, *Influence of potential well depth on nonlinear tristable energy harvesting*, Applied Physics Letters, 106, 173903, http://dx.doi.org/10.1063/1.4919532
19. Zhao, D., Gan M.Y., Zhang, C.H., Wei, J.D., Liu, S.G., 2018, *Analysis of broadband characteristics of two degree of freedom bistable piezoelectric energy harvester*, Materials Research Express, 5(8), 085704
20. Wang, H.Y., Tang, L.H., 2017, *Modeling and experiment of bistable two-degree-of-freedom energy harvester with magnetic coupling*, Mechanical Systems and Signal Processing, 86, pp. 29-39.
21. Wang, G.Q., Zhao, Z.X., Liao, W.H., Tan, J.P., Ju, Y., Li, Y., 2020, *Characteristics of a tri-stable piezoelectric vibration energy harvester by considering geometric nonlinearity and gravitation effects*, Mechanical Systems and Signal Processing, 139, 106571.
22. Zhu, P., Ren, X.M., Qin, W.Y., Yang, Y.F., Zhou, Z.Y., 2017, *Theoretical and experimental studies on the characteristics of a tri-stable piezoelectric harvester*, Archive of Applied Mechanics, 87, pp. 1541-1554.
23. Yang, T., Cao, Q.J., 2019, *Dynamics and performance evaluation of a novel tristable hybrid energy harvester for ultra-low level vibration resources*, International Journal of Mechanical Sciences, 156, pp. 123-136.
24. Zhou, Z.Y., Qin, W.Y., Yang, Y.F., Zhu, P., 2017, *Improving efficiency of energy harvesting by a novel penta-stable configuration*, Sensors & Actuators: A. physical, 265, pp. 297-305.
25. Rui, X.B., Zhang, Y., Zeng, Z.M., Yue, G.X. Huang, X.J., 2020, *Design and analysis of a broadband three-beam impact piezoelectric energy harvester for lowfrequency rotational motion*, Mechanical Systems and Signal Processing, 149, 107307.
26. Wang, Y.L., Yang, Z.B., Cao, D.Q., 2021, *On the offset distance of rotational piezoelectric energy harvesters*, Energy, 220, 119676.
27. Khameneifar, F., Moallem, M., Arzanpour, S., 2011, Modeling and analysis of a piezoelectric energy scavenger for rotary motion applications, Journal of Vibration and Acoustics, 133, 011005.
28. Zhang, Y.S., Zheng, R.C., Nakano, K., Cartmell, M.P., 2018, *Stabilising high energy orbit oscillations by the utilisation of centrifugal effects for rotating-tyre-induced energy harvesting*, Applied Physics Letters, 112, 143901.
29. Mei, X.T., Zhou, S.X., Yang, Z.C., Kaizuka, T., Nakano, K., 2019, *A tri-stable energy harvester in rotational motion: modeling, theoretical analyses and experiments*, Journal of Sound Vibration, 469, 115142.
30. Man, D.W., Zhang, Y., Xu, G.Z., Kuang, X.C., Xu, H.M., Tang, L.P., Han, T.T., 2023, *Improving energy harvesting from low-frequency excitations by a hybrid tri-stable piezoelectric energy harvester*, Alexandria Engineering Journal, 76, pp. 153-165.

Appendix

$$K_{\mathrm{c}} = m_0\left\{r\int_0^l (l-x)\phi_1'(x)^2\,\mathrm{d}x + \frac{1}{2}\int_0^l (l^2-x^2)\phi_1'(x)^2\,\mathrm{d}x - \int_0^l \phi_1(x)^2\,\mathrm{d}x\right\}$$
$$+m_{\mathrm{f}}\left[r\int_0^l \phi_1'(x)^2\,\mathrm{d}x - \phi_1(0)^2\right] + m_{\mathrm{t}}\left[(l+r)\int_0^l \phi_1'(x)^2\,\mathrm{d}x - \phi_1(l)^2\right]$$

$$\chi = m_0\int_0^l (x+r)\phi_1(x)\mathrm{d}x + m_{\mathrm{f}} r\phi_1(0) + m_{\mathrm{t}}(l+r)\phi_1(l) - m_{\mathrm{t}} e_{\mathrm{f}}\phi_1'(0) + m_{\mathrm{t}} e_{\mathrm{t}}(l+r)\phi_1'(l)$$

$$\vartheta = Y_{\mathrm{p}} b d_{31}\left(h + \frac{t_{\mathrm{p}}}{2}\right)\int_0^l \phi_1''(x)^2\,\mathrm{d}x\,,$$

$$\Gamma = m_0\int_0^l \phi_1(x)\mathrm{d}x + m_{\mathrm{t}}\phi_1(l) + m_{\mathrm{f}}\phi_1(0)\,,$$

$$C_{\mathrm{p}} = \frac{bl\varepsilon_{33}^{\mathrm{S}}}{2t_{\mathrm{p}}}$$